



Damage localization for composite structure using guided wave signals with Gramian angular field image coding and convolutional neural networks



Yunlai Liao^a, Xinlin Qing^{a,*}, Yihan Wang^a, Fanghong Zhang^{b,*}

^a School of Aerospace Engineering, Xiamen University, Xiamen 361102, China

^b National Center for Applied Mathematics, Chongqing Normal University, Chongqing 401331, China

ARTICLE INFO

Keywords:

Guided wave
Damage localization
Composite structures
Gramian angular field
Convolution neural network

ABSTRACT

Accurate detection of damage in composite structures is of great significance to ensure safe service and avoid catastrophic accidents. In this paper, a novel damage diagnosis method, integrating guided wave (GW)-based structural health monitoring (SHM) with Gramian angular field (GAF) image coding and convolutional neural networks (CNNs), is proposed to improve the accuracy of damage localization in composite structures. Firstly, an improved piecewise aggregate approximation (PAA) algorithm is proposed to achieve guided wave data compression and obtain a series of damage indexes (DIs) characterizing the damage for effectively improving the localization accuracy. Then, the multi-path fused DI sequences are converted into two-dimensional (2-D) images using GAF to take full advantage of the significant benefits of CNN in machine vision. Secondly, a CNN model is constructed to learn high-level feature representations and conduct damage location regression. Finally, the proposed method is tested and assessed on measured GW signal datasets with the addition of zero-mean Gaussian noise. The experimental results show that the mean relative error of the proposed method for damage localization on the invisible datasets is 3.59%. The proposed method demonstrates better generalization and localization performance than other selected state-of-the-art damage localization techniques.

1. Introduction

Advanced composite materials have been widely applied in the fields of aerospace, wind power generation, high-tech ships, etc., thanks to their light weight, high strength, and strong design flexibility. However, composite structures are susceptible to be damaged by external shocks and concentrated loads during the manufacture or service, and serious accidents may occur consequently if they are not inspected or maintained in time. Therefore, timely detection of damage in composite structures is of great significance to avoid sudden damage and structural failure, but it is particularly difficult to accurately localize a damage because of the inherent material non-homogeneity and anisotropy of composites, which makes damage localization challenging.

Structural Health Monitoring (SHM) technology is a revolutionary and innovative technique for assessing the health of composite structures [1–4]. Various methods have been proposed for damage detection and localization in composite structures using SHM technology [5–8], among which GW-based damage localization techniques have proven to

be more suitable [9–11]. These techniques usually require piezoelectric transducers (PZTs) to be mounted as actuators or sensors on the surface of the target structure [12,13]. Commonly, GW-based damage localization methods mainly include two steps: firstly, GW signals are recorded once before damage, which are called the baseline signals. After the damage occurs, the GW signals are measured once again and are referred to as the damage signals. Secondly, the overall difference between the baseline signals and the damage signals are analyzed and the damage indexes (DIs) characterizing the damage are extracted to localize the damage in the structure [14,15].

Different DIs, such as difference coefficients [16,17], energy ratios [18,19], and power spectral density [20], are often used as sensitive features of damage. For instance, Li et al. [16] has used the signal difference coefficient as an indicator of damage and utilized probabilistic ellipsoidal imaging for damage localization. Liu et al. [21] has used the Lyapunov exponent to define the DI and achieved localization of delamination damage in composite plates. While these methods could be used to identify the location of damage in composite structures, the

* Corresponding authors.

E-mail addresses: xinlinqing@xmu.edu.cn (X. Qing), fanghong.zhang@cqnu.edu.cn (F. Zhang).

definition of the DI is complex and the computation is time consuming. In addition, a large number of sensors is required. In practical applications, a solution with a simple DI calculation, a small number of sensors, and an effective damage localization scheme is highly preferred. Besides, due to the complex propagation characteristics of GW, such as dispersion, multimodality, and mode conversion, it is extremely challenging to extract robust DIs from the GW signals, which is further exacerbated in composite structures.

In recent years, CNNs are widely used and state-of-the-art diagnostic performance is achieved due to their powerful local feature extraction capabilities and flexible architecture [22,23]. The SHM of composite structures are increasingly focused on autonomous damage assessment and damage localization. In terms of autonomous damage assessment, Khan et al. [24,25] has used CNNs for autonomous detection and assessment of damage, and the results are satisfactory. Zhang et al. [26] has implemented autonomous assessment of composite folds based on CNNs. As for the damage localization, numerous studies [27–29] have utilized one-dimensional (1-D) CNNs to establish a mapping relationship between the time series data and the damage location. However, these depth structure models based on time series data all use a 1-D convolution kernel, and the generalization performance and applicability of the models still need to be further improved [30]. Compared with 1-D CNNs, 2-D CNNs have significant advantages in terms of generalization and robustness. Rautela et al. [31] has fed the GW signals into the CNNs in the form of 1-D time series and 2-D images for training, and concluded that the prediction and generalization effect of the latter was better than that of the former. However, to introduce the advantages of CNNs in 2-D image processing to 1-D time series, the key technical problem to be broken through is to convert 1-D time series data into 2-D images. Numerous studies [31–33] have converted time series data into images by Continuous Wavelet Transform (CWTs) or Short-Time Fourier Transform (STFTs), and then fed the images into CNNs for training, thus enabling the damage localization. However, most of the previous approaches have their own limitations. For instance, it is difficult to select a universal mother wavelet in the CWTs. STFT is unable to cope with the frequency demands of non-stationary signal variations. In addition, all these conversion methods rely much on expert's knowledge [34]. Therefore, it is essential to explore a universal and easy-to-use mathematical conversion method to improve the image transformation.

To further improve the localization performance of CNNs, a large number of studies [35–37] have concatenated all propagation paths into a vector to provide more spatial information about the damage. Although this approach can effectively improve the localization performance of CNNs, the volume of data after the stitching of these paths is very large, which is not conducive to the subsequent processing of the network. For instance, with four sensors there are 12 sensing paths, which results in 72,000 points when each path contains 6,000 points. As the number of sensors increases, the number of points increases dramatically. In practice, the CNN network input data should be as low-dimensional as possible, but still retain the feature information of the damage. In other words, there is an urgent need for an efficient data compression method that can effectively compress data while still retaining useful information. In addition, most of the existing researches on damage localization have focused on the classification of known damage locations [38–41], while few researches have been carried out on the regression of arbitrary damage locations.

Motivated by the aforementioned limitations, in this study, GAF-CNN-CBAM-based approaches are used to localize the damage and validate the proposed method with experiments. The contributions of this paper are summarized as follows:

- (a) An improved piecewise aggregate approximation algorithm is proposed for reducing the dimensionality of the GW signals, which is also utilized to obtain a series of DIs that retains temporal information features.

- (b) The feasibility of combining GAF digital image coding techniques with CNNs is investigated for SHM of composite structures. To our knowledge, this is the first time that GAF digital image coding techniques and CNNs have been combined for health monitoring of composite structures.
- (c) A novel GAF-CNN-CBAM intelligent diagnosis method is proposed for GW-based damage localization in composite structures. With this GAF-CNN-CBAM method, high-level features of the input information can be efficiently extracted using convolutional layers and convolutional block attention modules to achieve regression of damage locations. Unlike traditional methods that use a classification form to achieve damage localization, one of the significant innovations of the proposed method is that it can directly regress the coordinates where the damage is located.

The remainder of the paper is structured as follows. In Section 2, the convolutional neural network and the convolutional block attention module are introduced. In Section 3, the architecture of the GAF-CNN-CBAM model is presented with detailed description of each sub-part. In Section 4, the experimental details are described. In Section 5, thorough analyses of the results are provided. In Section 6, several important conclusions are drawn.

2. Theory background

2.1. Convolutional neural network

CNN is a typical feedforward neural network, which essentially constructs multiple filters to perform feature extraction on the input data [42]. Typically, the CNN usually consists of an input layer, a convolutional layer, a pooling layer, and a full connection layer.

In the convolution layer, the input images are convolved with multiple convolution kernels. After adding the bias term and passing the activation function, a series of feature maps can be generated. Taking the m -th layer of convolution in the CNN model as an example, the convolution operation is formulated as

$$x_j^{\ell,m} = f \left(\sum_{i \in M_j^{\ell-1,m}} x_j^{\ell-1,m}(i) * k_{ij}^{\ell-1,m} + b_{ij}^{\ell-1,m} \right) \quad (1)$$

where $x_j^{\ell,m}$ denotes the value of the j -th neuron in the m -th frame of layer ℓ , $M_j^{\ell-1,m}$ denotes the j -th convolution area of the feature map in the m -th frame of layer $\ell-1$, $X_j^{\ell-1,m}(i)$ denotes the value of the j -th neuron in the m -th frame of layer ℓ , $k_{ij}^{\ell-1,m}$ denotes the convolution kernel, and $b_{ij}^{\ell-1,m}$ denotes the bias, and the symbol $*$ represents the convolution operation between the local area and the convolution kernel.

After the convolution, the activation function is essential. It enables the network to acquire a nonlinear expression of the input signals to make the learned features more dividable. Rectified Linear Unit (ReLU) is widely used as activation unit to accelerate the convergence of the CNNs. The formula of ReLU is described as

$$\xi_j^{\ell,m} = f(x_j^{\ell,m}) = \max\{0, x_j^{\ell,m}\} \quad (2)$$

where $\xi_j^{\ell,m}$ denotes the activation of $x_j^{\ell,m}$. After activation, it is common to add a pooling layer after the activation layer in the CNN architecture. The pooling layer is used to obtain a representation that is invariant to small transformations and distortions. The most commonly used pooling layer is max-pooling layer, and the max-pooling transformation is expressed as

$$P_j^{\ell+1,m} = \max_{(j-1)n+1 \leq k \leq jn} (\xi_j^{\ell,m}) \quad (3)$$

where $P_j^{\ell+1,m}$ denotes the value of the j -th neuron in the m -th frame of layer $\ell+1$. $k \in [(j-1)n + 1, jn]$, and n indicates the width of the pooling region.

Finally, the full connection layer integrates the advanced feature representations obtained alternately from the input images into a one-dimensional vector to realize the end-to-end learning process. Thus, the influence of feature position on classification or regression results is reduced and the robustness of the whole network is improved.

2.2. Convolutional block attention module

The convolutional block attention module (CBAM) is a kind of attention mechanism module that combines the two dimensions of the channel attention module and the spatial attention module [43]. In the channel attention module, each channel of the feature map is a feature detector. The channel attention module is concerned with the relationship of features between channels, mainly extracting meaningful content information from the input images and compressing the spatial orientation information of the input feature maps. The spatial attention module is concerned with the spatial relationship of features and focuses on extracting the location information of targets in the input images, complementing the channel attention module to select the content and location information of targets in the feature maps. With the two modules, the network focuses more on the important features of the images and suppresses unwanted regional responses.

Given an intermediate feature map $F \in R^{C \times H \times W}$ as input, CBAM sequentially infers a 1-D channel attention map $M_c \in R^{C \times H \times W}$ and a 2-D spatial attention map $M_s \in R^{C \times H \times W}$ as illustrated in Fig. 1. The overall attention process can be summarized as

$$F' = M_c(F) \otimes F \quad (4)$$

$$F'' = M_s(F') \otimes F' \quad (5)$$

where \otimes denotes the element-wise multiplication, F' indicates the channel-refined feature, and F'' is the final refined output.

3. The proposed methodology for damage localization based on GAF-CNN-CBAM

3.1. Framework overview

The framework of the proposed GAF-CNN-CBAM-based damage localization is shown in Fig. 2, which mainly includes the following four steps.

Step 1: Initial damage experiments are carried out on the test bench and raw GW signals are collected.

Step 2: The GW signals are compressed using an improved PAA algorithm, and a new time series is obtained after multi-path fusion. The new time series is then processed by GAF to obtain a 2-D image sample with preserved temporal feature information.

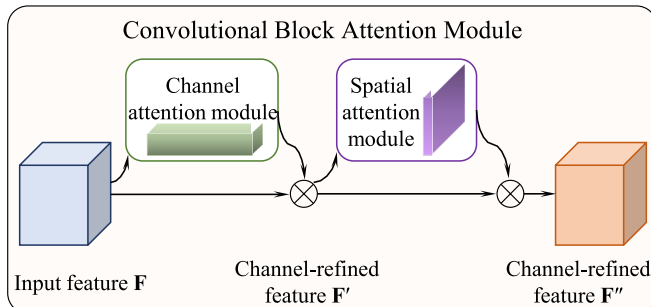


Fig. 1. Overview of CBAM.

Step 3: The sample set is constructed by combining the 2-D images and damage location coordinates into three categories: training, validation and test. The GAF-CNN-CBAM model is constructed layer by layer, and then the model is trained using training datasets and validation samples. Test datasets are input to the well-trained GAF-CNN-CBAM model, and location results are output.

Step 4: The location of damage is identified on the basis of the output results, and the performance of the model is assessed in terms of various metrics.

3.2. A novel series of DIs by using the improved PAA algorithm

Though the PAA algorithm is widely used due to its powerful data dimensionality reduction capability [44], it needs complex computations. In this paper, an improved PAA algorithm is proposed for dimensionality reduction of GW signals. Given a discrete GW signal $Y_m = Y(m\Delta t)$, for $m = 1, 2, 3, \dots, n$ with sampling interval Δt , due to the influence of uncertain factors such as manual operation and the changes of physical properties of the materials, the GW signals obtained at the same position coordinate could be quite different [45]. Hence, the baseline signals are introduced to exclude the effect of uncertainty. Assuming that the signal of the healthy plate is $Y_B = Y(m\Delta t)$ and the signal of the damaged plate is $Y_D = Y(m\Delta t)$, respectively, the GW signals of the healthy plate are subtracted from those of the damaged plate and the absolute value is taken, which can be expressed as

$$X_i = |Y_{Bi} - Y_{Di}| \quad (6)$$

where Y_{Bi} denotes the i -th value in the Y_B , Y_{Di} indicates the i -th value in the Y_D , and X_i is the i -th value in the X . The time series X is the absolute residual signal, i.e., the absolute value of the baseline signals subtracted from the damage signals, contains all the information about the damage.

This time series X of length n is represented by a sequence S of length z , and the k -th element of S is calculated by the following equation:

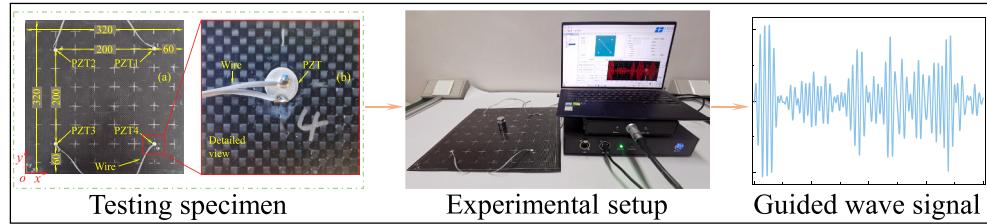
$$S_k = \frac{1}{M} \sum_{k=N}^{M+N} X \text{ for } k = 0, 1, 2, \dots, z-1 \quad (7)$$

where M denotes the signal selection length, and N is the jumping length. It should be noted that the signal selection length M should not be too large, to avoid strong low-pass filtering. In this paper, the signal selection length M is equal to the excitation signal length. Simply stated, in order to reduce the data from n dimensions to z dimensions, the data is divided into z equal frames. The average value of the data within the frame is calculated and this average value is substituted for the data within the whole frame. Averaging is beneficial because it enhances discriminative features that the segments share with each other and suppress random features caused by noise [46]. The flowchart of the improved PAA algorithm is illustrated in Fig. 3. Each value in the sequence S_z reflects the average of the absolute magnitude of the difference between the baseline signals and the damage signals for any segment. The larger the value is, the greater the damage (also known as DI) is, and vice versa. Thus, the sequence S_z is essentially a new sequence made up of z DI values. As can be seen from Eq. (6) and Eq. (7), the calculation of DIs is extremely simple. The innovation of the improved PAA algorithm compared to the PAA algorithm [44] is that there is an overlap between the sequence frames, thus ensuring correlation between the data frames. From the process of deriving the sequence S_z , it is clear that the S_z sequence still retains the temporal information feature, which is important for damage localization.

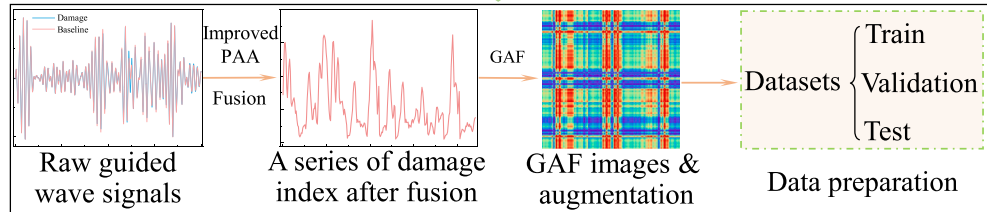
3.3. GAF image generation

To make the 1-D GW signals of PZT sensors maintain local temporal relationships and take full superiority of the obvious advantages of neural networks in machine vision, the GAF [47] is introduced to

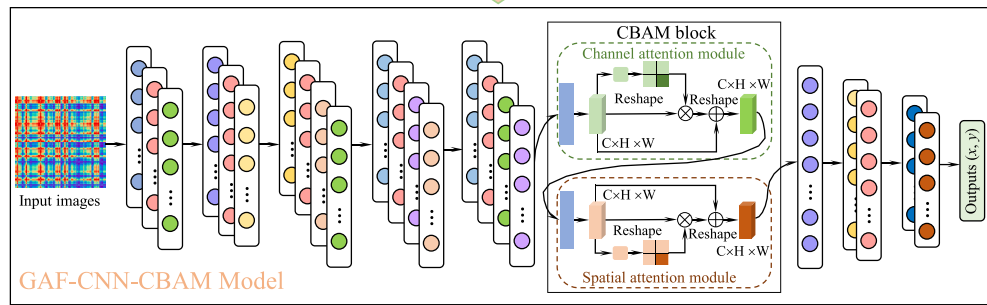
1. Guided wave signals acquisition



2. Generating samples



3. GAF-CNN-CBAM Model



4. Results

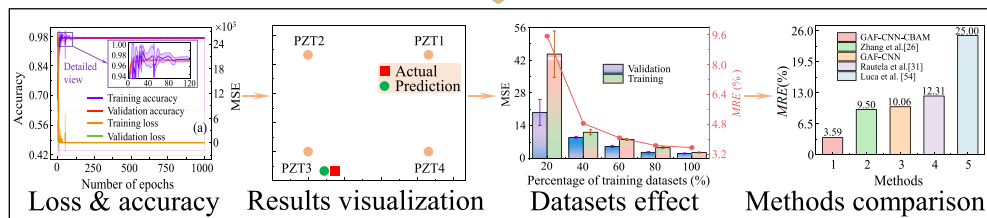


Fig. 2. Flowchart of damage localization based on GAF-CNN-CBAM in composite structures.

transform 1-D time series into 2-D images representations. Notably, this is the first time that GAF has been applied to health monitoring of composite structures based on GW. Given a set of time series X , the original signal X is normalized into the interval $[-1, 1]$ using the minimum and maximum normalization method and then the normalized signal \tilde{X}_i is obtained. The normalized signal \tilde{X}_i can be represented as

$$\tilde{X}_i = \frac{(x_i - \min(X)) + (\max(X) - \min(X))}{\max(X) - \min(X)} \quad (8)$$

Then, the transformation function $f(\cdot)$ is used to transform the normalized signal \tilde{X}_i to the polar coordinate system, which represents the cosine of the normalized amplitude and the radius of time t , as shown in Eq. (9).

$$f(\tilde{x}_i, t_i) = [\phi_i, r_i] \text{ where } \left\{ \begin{array}{l} \phi_i = \arccos(\tilde{x}_i), \tilde{x}_i \in \tilde{X} \\ r_i = t_i \end{array} \right. \quad (9)$$

where ϕ denotes the angle value, and r indicates the radius. By calculating the cosine value of the difference in angles between different points, the GAF matrix can be expressed as

$$GAF = \begin{pmatrix} \cos(\phi_1 - \phi_1) & \cdots & \cos(\phi_1 - \phi_n) \\ \vdots & \ddots & \vdots \\ \cos(\phi_n - \phi_1) & \cdots & \cos(\phi_n - \phi_n) \end{pmatrix} \quad (10)$$

It should be noted that the matrix in Eq. (10) has two significant properties. Firstly, the value range of the converted angle ϕ is $[0, \pi]$, and the cosine value decreases monotonically within this range. Given time series data, the map yields one and only one result in the polar coordinate system with a unique inverse map. Secondly, unlike cartesian coordinates, polar coordinates preserve absolute temporal relations. After encoding the time-series data into a polar coordinate system, the correlation coefficient between time intervals can be easily extracted considering the trigonometric difference between points. In this way, the GAF provides a new representation style that can preserve the local temporal relationship in the form of temporal correlation as the timestamp increases, which plays a significant role in damage localization. The two advantages facilitate the use of GAF. For the compressed and fused GW data, the GAF is used to convert the data into images which are the input of the GAF-CNN-CBAM model.

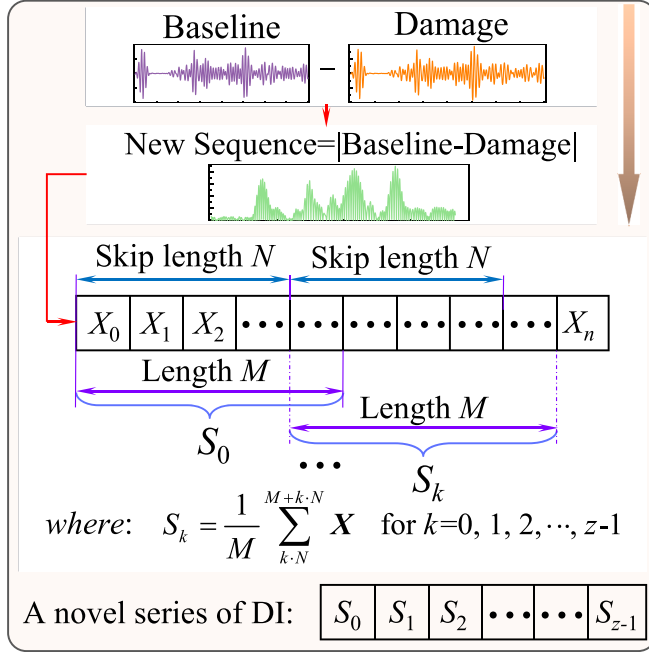


Fig. 3. Flowchart of the improved piecewise aggregate approximation algorithm.

3.4. The proposed GAF-CNN-CBAM model for damage localization

In this section, the architecture of the proposed GAF-CNN-CBAM model is discussed. Fig. 4 shows that the network consists of ten blocks and a CBAM block for automatically extracting discriminative features from the GAF images of the damage localization cases. The detailed architecture of the proposed network is summarized as shown in Table 1. Specifically, the network consists of an input layer, 13 convolutional layers (CLs), six max-pooling layers (MPLs), a normalization layer (NL), a flatten layer (FL), three full connection layers (FCLs), an output layer (OL), and a convolutional block attention module (CBAM). The GW signals are compressed and fused into a new time series, and then converted by GAF to 2-D images which are designed as the input of the GAF-CNN-CBAM model. The output of the model is a vector composed of the horizontal and vertical coordinates corresponding to each damage location of the CFRP plate.

In this model, the CLs and the MPLs are alternatively arranged to gradually reduce the height and width of the images while increasing their depth. All CLs use a 3×3 kernel to quickly extract learnable patterns and learn features. The size of the MPLs is 2×2 , which avoids losing too much meaningful information while reducing the size of the

Table 1
The proposed network configuration.

Block Name	Layer Name	Layer Description
Block 1	Input layer	128×128 3-channel GAF image
Block 2	Conv2D	Convolution filter 3×3 , strides 1
	Conv2D	Number of filter = 16, ReLU
	Maxpooling	Max-pooling filter 2×2 , strides 2
Block 3	Conv2D	Convolution filter 3×3 , strides 1
	Conv2D	Number of filter = 32, ReLU
	Maxpooling	Max-pooling filter 2×2 , strides 2
Block 4	Conv2D	Convolution filter 3×3 , strides 1
	Conv2D	Number of filter = 64, ReLU
	Conv2D	Max-pooling filter 2×2 , strides 2
Block 5	Conv2D	Convolution filter 3×3 , strides 1
	Conv2D	Number of filter = 128, ReLU
	Conv2D	Max-pooling filter 2×2 , strides 2
Block 6	Conv2D	Convolution filter 3×3 , strides 1
	Conv2D	Number of filter = 256, ReLU
	Conv2D	Max-pooling filter 2×2 , strides 2
CBAM block	Maxpooling	/
	Channel attention	/
	Spatial attention	/
	BatchNormalization	/
Block 7	Maxpooling	Max-pooling filter 2×2 , strides 2
	Flatten	/
Block 8	Full connection	Dense = 512, ReLU
Block 9	Full connection	Dense = 512, ReLU
Block 10	Full connection (Output)	Dense = 2, linear

learning patterns. In particular, a two-pixel stride halves the height and width of the image, but the depth of the image remains unchanged. The FL is employed to transform the output of the last MPL into a 1-D feature map. Then, three FCLs are added, and the network utilizes a linear layer as the last layer to achieve damage localization and output the localization results.

4. Experimental validation

4.1. Fabrication of testing specimen

To validate the theoretical models and the proposed damage localization methodology for composite structures, a carbon fiber reinforced polymer (CFRP) plate with a layup of $[0/90/90/0]_s$ was manufactured. The CFRP plate was made of T300 woven preprints, and the CFRP plate consisted of eight plies whose thickness was 0.2 mm, and the total thickness of the plate was 1.6 mm. The preprints had been vacuumed and cured in an autoclave at 120 °C for three hours. The dimensions of the final CFRP plate were 320 mm \times 320 mm \times 1.6 mm. The sensor array consisted of four piezoelectric transducers, which were attached to the CFRP plate with AB epoxy adhesive and were responsible for exciting

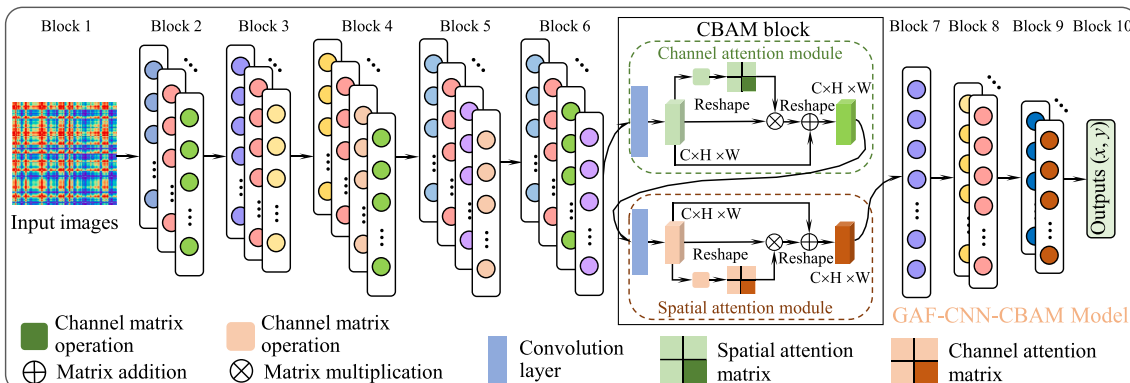


Fig. 4. The architecture of the proposed GAF-CNN-CBAM model used for damage localization.

and receiving guide wave. The naming of the PZTs (starting from PZT1, counter-clockwise) and the coordinates of the piezoelectric transducers are shown in [Table 2](#). The PZTs used in the experiments are PZT-5A (S33), which are made of lead pick titanate and produced by China Railway Academy of Science Group Co. The key elastic parameters are shown in [Table 3](#).

The illustration of the prepared CFRP composite specimen and the sensor position are shown in [Fig. 5\(a\)](#) while the detailed view of the PZT is shown in [Fig. 5\(b\)](#).

4.2. Guided wave signal acquisition and datasets

The experimental system consists of a CFRP plate, a model defect, a piezoelectric sensor array, a monitoring system and a computer, as shown in [Fig. 6\(a\)](#). The monitoring system developed by Dalian Junsheng Technology Co., includes a 128-channel switch system and a host system. The role of the 128-channel switching system is the switching and connecting of channel signals. The host system integrates the functions of signal generation, power amplification, high-speed acquisition, band-pass filtering and so on, and the computer is for system parameters setting, real-time display and data storage of GW signals. More detailed information on the monitoring system can be found in [1], and the technical parameters are shown in [Table 4](#).

In this paper, only four cylindrical PZTs with a diameter of eight mm were utilized to receive GW signal propagating in the CFRP plate, which were bonded in a parallel manner to the CFRP plate and formed 12 propagation paths. Given the high price and limited resources, collecting data on a real damaged CFRP plate is not practicable. Therefore, a model defect with a diameter of 14 mm was used to simulate the damage [21]. A five-cycle tone-burst input signal with an excitation frequency of 100 kHz was used for the excitation as shown in [Fig. 6\(b\)](#). The length of the GW signal localization was based on the following criterion: After the GW had passed through the damage, the scattered wave could still propagate to all sensors. The damage localization was achieved by changing the coordinates of the model defect on the CFRP plate. It should be noted that there was only one model defect in the CFRP plate in each experiment. For each model defect, 12 GW wave signals were collected from 12 propagation paths via the monitoring system, with a sampling frequency of 12 MHz.

The process of GW signal acquisition is listed in [Table 5](#) and consists of nine phases. In the first phase, 15 baseline measurements of the intact structure were recorded. After that, the model defect was placed at 49 different positions on the CFRP plate. These measurements correspond to 49 damage locations in damage set A as shown in [Fig. 7\(a\)](#). In each case, only a single defect model was attached to the structure at the same time. Another 15 baseline measurements were recorded in the third phase, followed by measurements of damage set B in the fourth phase. The measurements of the fifth to eighth phases were almost identical to those of the first to fourth phases, except for the number and location of damage. In the last phase, damage locations in damage set E were measured as shown in [Fig. 7\(b\)](#). It should be noted that these 16 points are not included in the sets A, B, C, and D. Finally, some points in the sets A, B, C, D and all points in the set E were used as test datasets for the subsequent GAF-CNN-CBAM model. The rest of the model defects were used as the training datasets.

The GW wave signal acquisition took about three days. The large number of baseline measurements enabled the analyses of statistical variations and also played a certain role in temperature compensation [48].

Table 2
Coordinates of the piezoelectric transducers.

Label	PZT1	PZT2	PZT3	PZT4
Coordinate (mm)	(260, 260)	(60, 260)	(60, 60)	(260, 60)

Table 3
Key elastic parameters of PZT-5A.

Item	Parameter	Value
$s_{11}^E (\times 10^{-12} \text{m}^2/\text{N})$	Compliance coefficient at constant electric field	16.4
η	Mechanical loss factor	0.01
$\epsilon_{33}^T / \epsilon_0$	Relative permittivity at constant stress	1920
δ	Dielectric loss factor	0.012
$d_{31} (\times 10^{-12} \text{C/N})$	Piezoelectric strain coefficient	-200
ν	Poisson's ratio	0.35
$\rho (\text{kg/m}^3)$	Density	7750
$h (10^{-3}\text{m})$	Thickness	0.48
$a (10^{-3}\text{m})$	Radius	4

5. Results and discussion

5.1. Analysis and image generation of guided wave signals

The interaction between GW signals and damage was investigated. The experimental GW signals (in time-domain) were obtained from all the four sensors for different damage locations. For page limitations, [Fig. 8\(a\)–\(f\)](#) show only the waveforms of the GW signals along the six propagation paths where the damage is located at coordinates (200, 120), (Ref. [Fig. 7](#)). The six propagation paths corresponding to [Fig. 8\(a\)–\(f\)](#) are shown in [Fig. 8\(g\)](#), and the absolute scattering signals of these six propagation paths are obtained using Eq. (6) as shown in [Fig. 8\(h\)](#). It can also be demonstrated that the higher the amplitude of the absolute scattering signal is, the closer it is to the damage, which is capable of commendably reflecting the damage propagation behavior. Although the GW signals under different propagation paths can be received by the PZT sensors, it is complicated and difficult to distinguish the signals due to complex phenomena such as modal changes, scattering attenuation and waveform aliasing after propagating through different paths. Therefore, it is very difficult to directly extract damage characteristics from the original GW signals, and it is also unreliable to rely on the original GW signals for damage localization.

In the experiments, the GW signals were processed using the improved PAA algorithm to obtain a series of DIs, and GAF was performed on the concatenated series to obtain 2-D images as the input of the GAF-CNN-CBAM model. The GW signals of each propagation path for each experiment were compressed using the improved PAA algorithm proposed in [Section 3.2](#). Examples of the DI sequences of the several GW signals corresponding to different damage locations under the same propagation path are illustrated in [Fig. 9](#). It can be found that the series of DIs contains 22 points, which means that the original GW signals were compressed by roughly 273 folds using the improved PAA algorithm, but still maintained the time information of the damage. This reflects the powerful capability of the improved PAA algorithm in data compression. In addition, the series of DIs obtained from different propagation paths have distinct favoritism for the locations of different damages. More specifically, for the propagation path (PZT1-PZT2), Damage 11 obstructs the straight path between PZT1 and PZT2, and it shows a higher DI. Similarly, the same results are also obtained for the propagation paths (PZT1-PZT4), (PZT2-PZT3) and (PZT3-PZT4), respectively. It can be inferred that the changes in the series of DIs are more pronounced when the damage falls in the direct propagation path of the GW signals. Therefore, using multiple plots as shown in [Fig. 9](#), it is possible to qualitatively identify which propagation path the damage is closer to.

Afterwards, these 12 series of DIs were concatenated in a certain order to form a new series containing a total of 264 points. This process was considered as the fusion of GW signals from multi-propagation paths [35]. Further, GAF is performed on the concatenated series to obtain a 2-D image as the input of the GAF-CNN-CBAM model. Examples of the GAF of concatenated series in four scenarios are illustrated in [Fig. 10](#) for the limitation of pages. Each damage location corresponds to a unique GAF image. Taking damage (120, 260) and damage (120, 280) as an

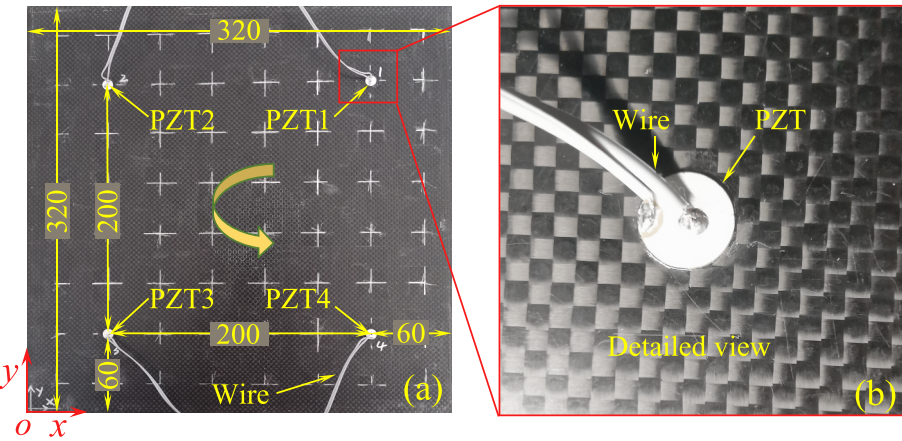


Fig. 5. CFRP composite specimen used in the experiments. (a) top view, (b) detailed view.

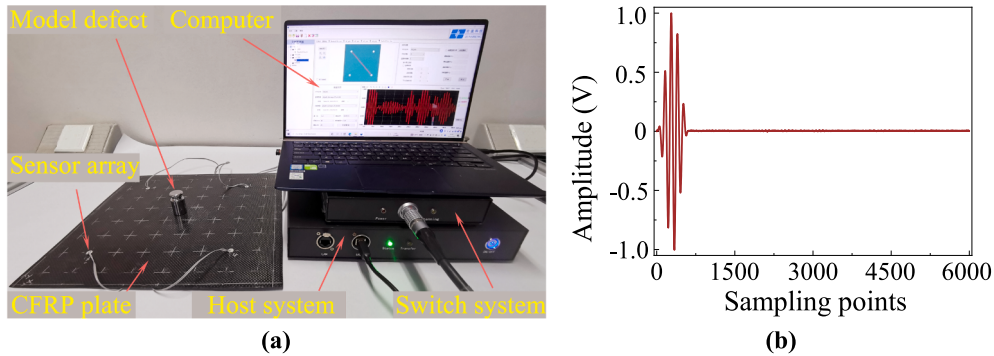


Fig. 6. (a) Guided wave signal measuring platform used in the experiments. (b) The five-cycle tone-burst input signal.

Table 4
Technical parameters of the monitoring equipment.

Technical parameter	Index
Excitation Frequency Range	10 kHz ~ 1000 kHz
Conversion Rates	48 MHz
Output Voltage Range	Min: ±10 V; Max: ±60 V
Memory	32,000 Samplings
Sampling Rates	6, 12, 24, 48 MHz/s
Resolution	12-bit
ADC Range	±1 V
Gain Adjustment Range	10 db ~ 40 db, step: 1 db

Further, the data augmentation was carried out by adding zero-mean Gaussian noise to the normalized GAF images using the Python toolkit “util” [49]. The zero-mean Gaussian noise added to the normalized image had a mean of zero and standard deviations of 0.003 and 0.006, respectively. Adding zero-mean Gaussian noise could simulate part of the environmental noise, effectively enriching the information of the training samples and helping the network learn more robust features, thus improving the robust performance of the network [50]. The image resizing and augmentation process are also represented in Fig. 10. In the process, a total of 10,620 images were collected for all the model defects.

5.2. The learning process and results of damage localization in the GAF-CNN-CBAM model

This section introduces the learning process and the results of initial damage localization using GAF images in the proposed GAF-CNN-CBAM model. The GAF feature images extracted from the GW signals were divided into a training set, a validation set, and a test set according to a ratio of 7: 2: 1. These images together with corresponding damage locations were then introduced sequentially for training the model. The model training and testing were performed on a TensorFlow 2.4.1 package with Python 3.7.13 environment and desktop, with two Intel (R) Xeon (R) Gold 6230R (CPU), NVIDIA GeForce RTX 3080Ti graphics processing units (GPUs), and running on a Windows 10 (64-bit) operating system with 512 GB DDR4 memory. The mean square error (MSE) loss function was used to train the model, and the Rectified linear unit (ReLU) was used as an activation function to enhance computational efficiency. The initial learning rate was 0.001, and the learning rate became one-tenth of the previous one for every 30 epochs of training. The model was trained with a mini-batch stochastic optimization using an adaptive moment estimation (Adam) optimizer [51] and batch size of

example, the distance between the two damages is only 20 mm, but the difference is dramatically in the corresponding GAF images. Initially, the size of each image was [264 × 264 × 3] (length × width × number of channel). To reduce computations, these images were resized to [128 × 128 × 3] pixel in Python, and the resized image data were normalized.

Table 5
Process of GW signals acquisition.

Phase	Description
1	15 baseline measurements
2	Damage set A (49)
3	15 baseline measurements
4	Damage set B (56)
5	15 baseline measurements
6	Damage set C (56)
7	15 baseline measurements
8	Damage set D (60)
9	Damage set E (16)

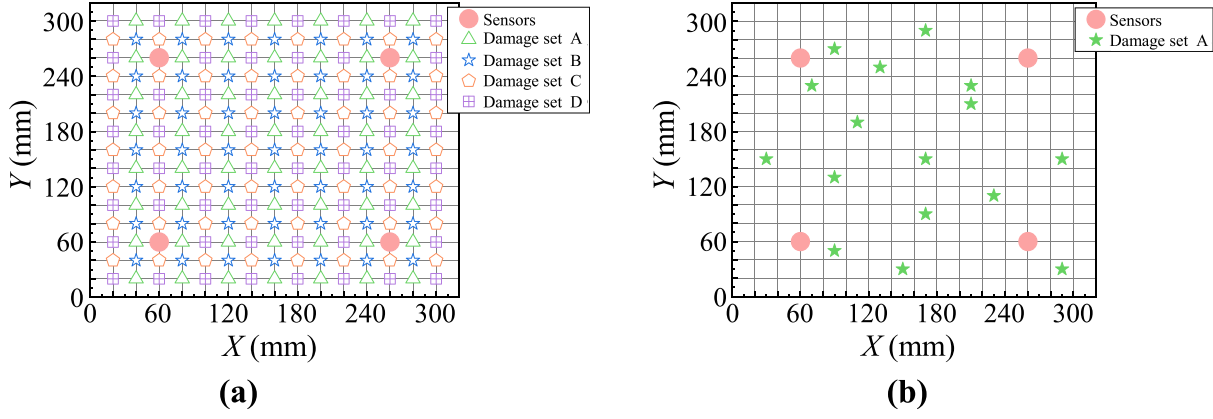


Fig. 7. Schema of the CFRP plate with model defect positions. (a) Damage sets A, B, C, D; (b) Damage set E.

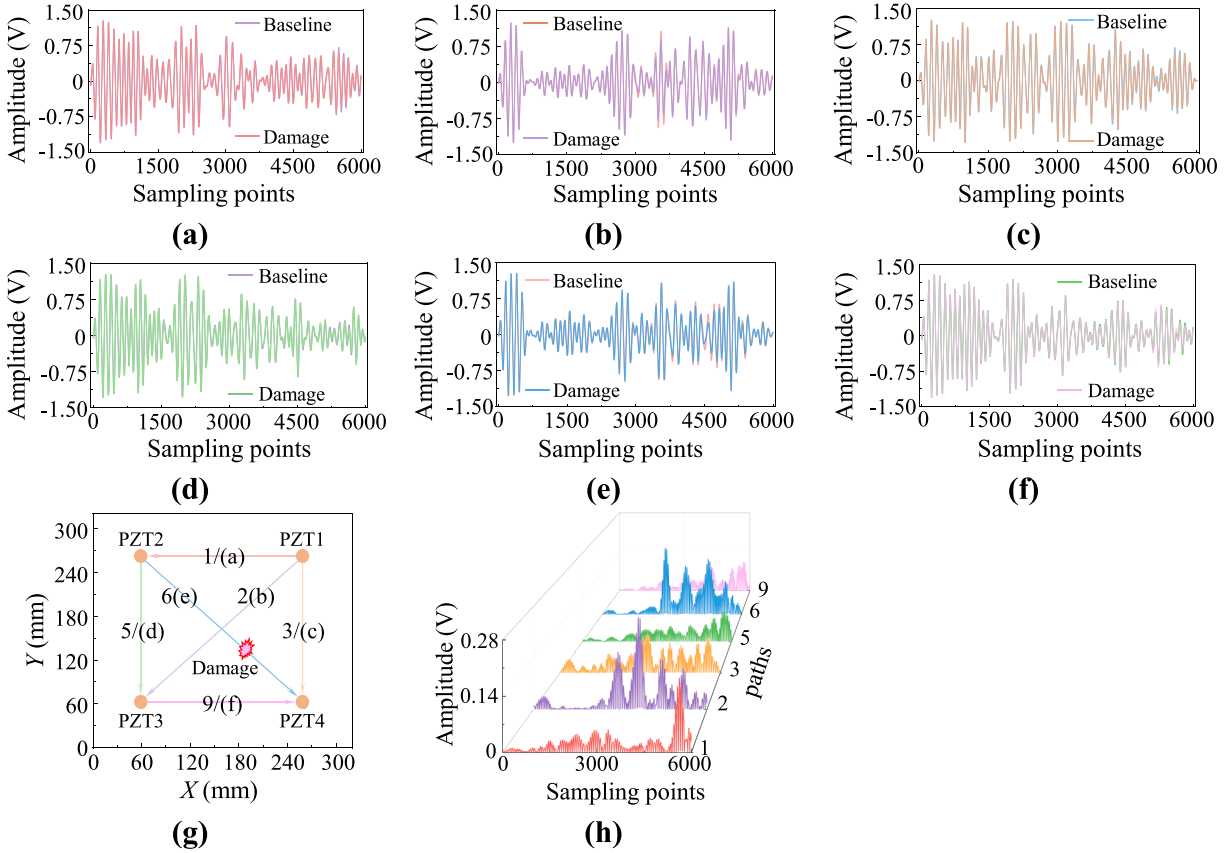


Fig. 8. The raw guided wave signals for different propagation paths when the damage is located at (200, 120). (a) Path PZT1-PZT2, (b) Path PZT1-PZT3, (c) Path PZT1-PZT4, (d) Path PZT2-PZT3, (e) Path PZT2-PZT4, (f) Path PZT3-PZT4, (g) Schematic diagram of the propagation paths, (h) Absolute scattering signals of different paths.

64 to minimize MSE between the model output damage location and the actual damage location. In addition to MSE, the metrics, such as mean absolute percentage error (MAPE), mean absolute error (MAE), and coefficient of determination (R^2), were also used to quantify the proposed model. Notably, three trials were conducted for each experiment to reduce the effect of randomization. It took on average 18,947 s on an NVIDIA GeForce RTX 3080Ti to complete the training per GAF-CNN-CBAM.

The variation of the accuracy and loss for GAF images generated from the raw GW signals with the number of epochs under the proposed GAF-CNN-CBAM model is shown in Fig. 11(a). The solid curve shows the mean and the shaded area shows the standard deviation. It can be clearly

seen that after 120 epochs, the validation accuracy and training accuracy of the model remain a constant at 97.27%, indicating that the model has completed its training without overfitting. The MAPE, MAE, and R^2 curves are shown in Fig. 11(b)–(d), respectively. A MAPE of 1.13 percent for training and 1.23 percent for validation, a MAE of 1.25 mm for training and 1.27 mm for validation, whereas a R^2 of 0.99 for training and 0.99 for validation are noted. The proposed model is capable with low MSE, MAPE, MAE, and a high R^2 . Accordingly, these metrics demonstrate the accuracy and validity of the proposed model in damage localization.

For testing the localization performance of the well-trained GAF-CNN-CBAM model, the model was tested on the test dataset. The

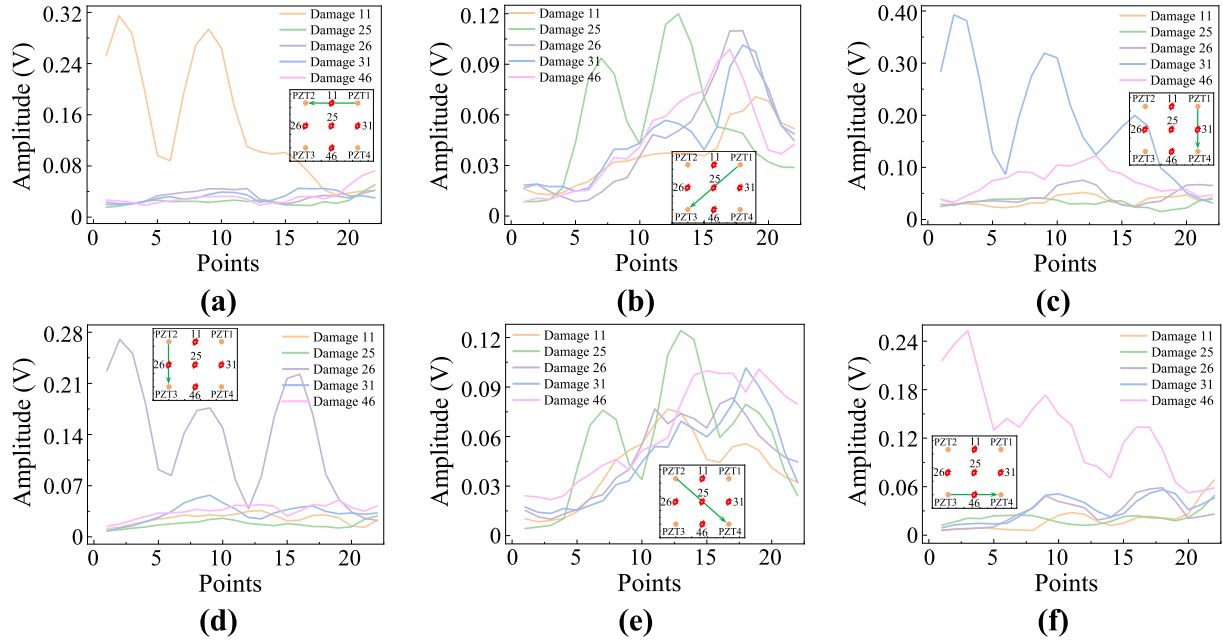


Fig. 9. The series of DIs of different damage locations under the same propagation path. (a) Path of PZT1-PZT2, (b) Path of PZT1-PZT3, (c) Path of PZT1-PZT4, (d) Path of PZT2-PZT3, (e) Path of PZT2-PZT4, (f) Path of PZT3-PZT4.

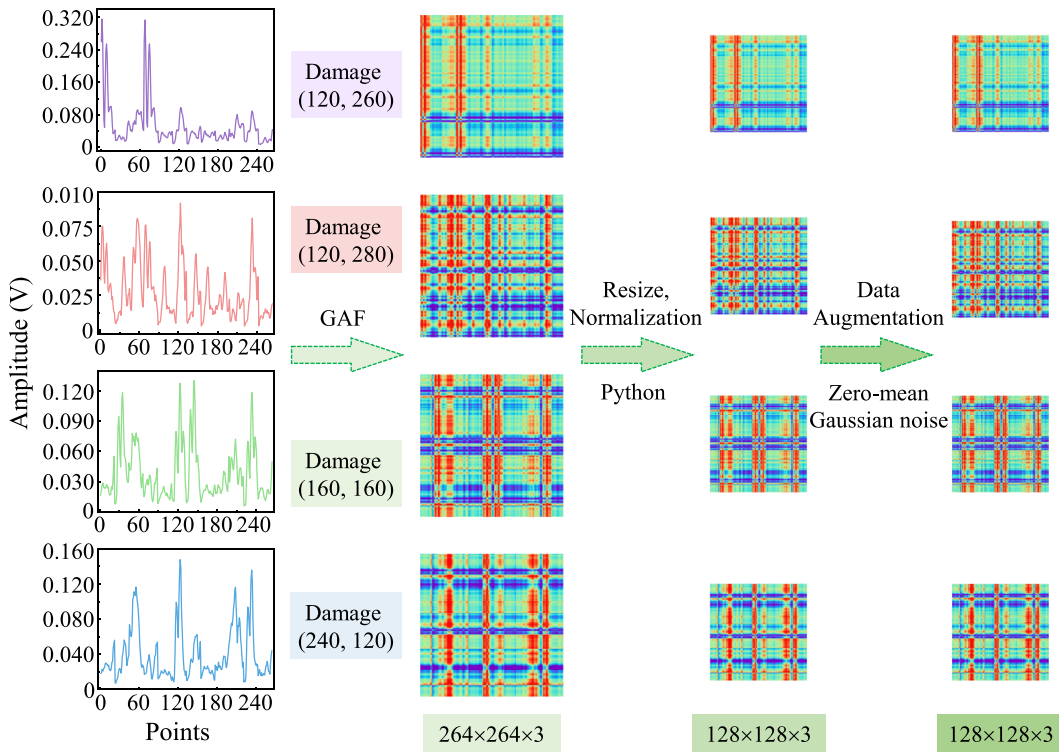


Fig. 10. A typical representation of the GAF images, resizing the images and image augmentation of DI series signals corresponding to damage (120, 260), damage (120, 280), damage (160, 160), and damage (240, 120).

detailed damage localization results for eight damage scenarios are given in Table 6 under the limitation of the page, and the visualization of damage localization results are shown in Fig. 12. It can be intuitively seen that the proposed method accurately predicts the damage location, regardless of whether the damage is located in outside or inside the region covered by propagation paths. During the experiments, the damages in Fig. 12(a)–(d) are the points in the training set A, B, C, or D, and the location results are shown in Table 6(a)–(d). The scale of the

zero-mean Gaussian noise added to the data in these test points is different from that in the training set. From the test results, although these test points are disturbed by noise, the proposed model can still learn features from the GAF images containing noise and accurately identify the damage location. While the damages in Fig. 12(e)–(h) are points in the damage set E, which are located near some of the points in the training set A, B, C, or D. The proposed method can also accurately identify the damage location and the details of the location results are

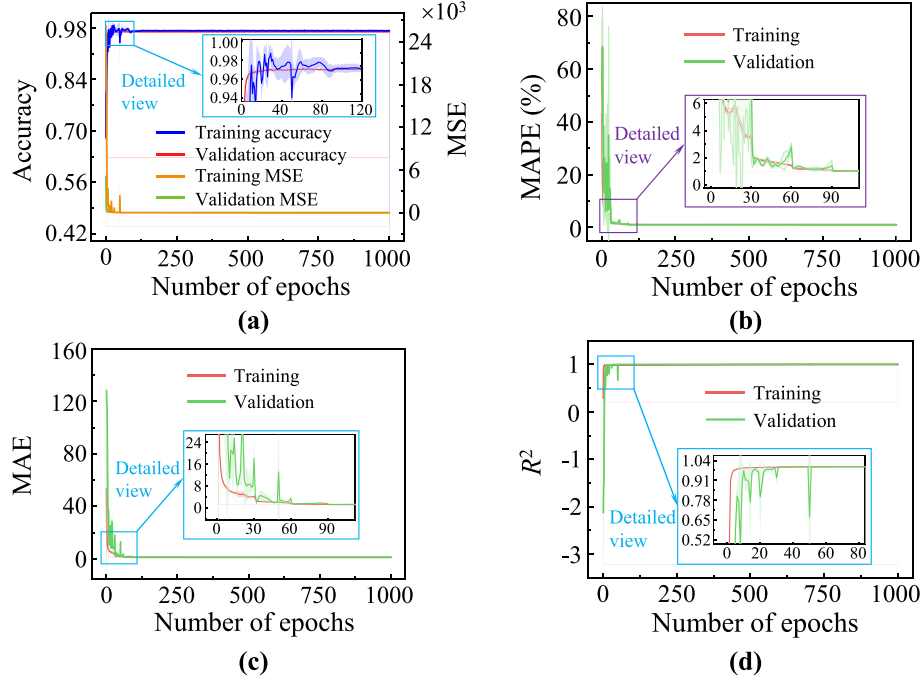


Fig. 11. The regression performance metrics curves of the GAF-CNN-CBAM model. (a) The learning curves of the proposed GAF-CNN-CBAM model on GAF image samples, (b) MAPE curves, (c) MAE curves, (d) R^2 curves.

Table 6
Examples of damage localization results.

Damage	Actual damage	Predicted damage	RE (%)
a	(20, 240)	(20.44, 240.42)	0.30
b	(40, 40)	(42.65, 39.99)	1.33
c	(120, 100)	(122.04, 99.55)	1.02
d	(180, 220)	(178.68, 222.38)	1.20
e	(90, 50)	(80.69, 51.81)	4.74
f	(130, 250)	(125.64, 264.51)	7.58
g	(230, 110)	(240.34, 111.36)	5.21
h	(290, 30)	(304.47, 27.52)	7.34

presented in Table 6(e)–(h). Therefore, the above test results indicate that the proposed method in this paper has robustness.

To assess the effect of localization, the relative errors (REs) are

employed to assess the damage localization performance [52]. The RE can be represented as

$$RE = \frac{\sqrt{(x_A - x_P)^2 + (y_A - y_P)^2}}{L} \times 100\% \quad (11)$$

where (x_A, y_A) denotes the actual damage location, (x_P, y_P) indicates the predicted damage location, and L denotes the distance between two sensors ($L = 200$ mm). The details of the calculated RE values are shown in Table 6. As can be seen from the table, the maximum relative error of the damage localization results is 7.58%. The results clearly show that the proposed method is capable of accurately localizing the damage.

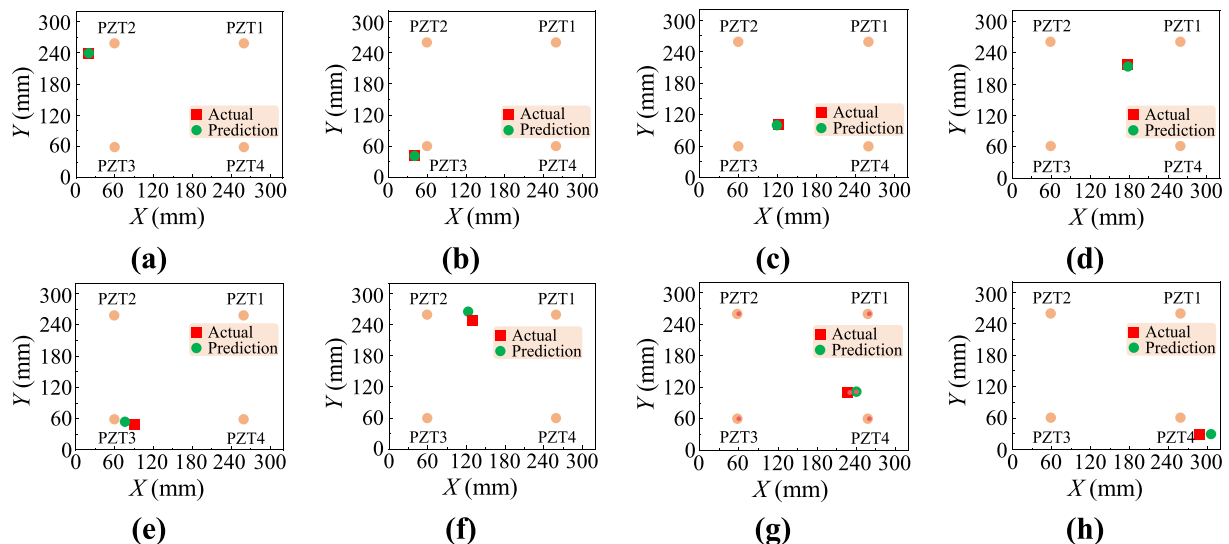


Fig. 12. Examples of the visualization of damage localization results in a few randomly selected testing cases.

5.3. The effects of training datasets size and skip length N on the model

There are several parameters in the proposed method, i.e., the length M and the skip length N of the improved PAA algorithm, and the datasets size. Here, the effects of these three parameters on the regression performance are discussed. In this study, three trials were carried out for each experiment to reduce the effects of randomness.

5.3.1. Effects of datasets size

The size of the training datasets affects the quality of the machine learning model [53], so the relationship between the MAPE loss of the proposed model and the training datasets with different sizes was investigated. Specifically, 20%, 40%, 60%, 80%, and 100% of the total datasets were selected to obtain five well-trained models for the proposed method in this paper, respectively. Furthermore, in order to maintain stable network performance, 3-fold cross-validation of the selected percentages of training data was performed according to Ref. [39]. The diagnosis results of the five well-trained models are displayed in Fig. 13. The training loss and testing loss are averaged by three trials, and the positive error bars show the standard deviations. Obviously, the MAPE value under these five different percentages of training samples exhibit distinct sizes. When the percentage of training datasets increases, the losses decrease and the corresponding standard deviations decrease as well. In addition, when a training dataset is small, overfitting phenomenon appears. Taking the model with 20% training datasets as an example, the difference between the training MAPE and the testing MAPE is large. This reflects that overfitting of the model has occurred. When the number of training datasets increases, the gap between the training MAPE and the testing MAPE loss decreases gradually and the overfitting phenomenon disappears gradually. It means that a GAF-CNN-CBAM model with better localization performance can be trained with more training datasets.

After that, the five well-trained models were used to predict the eight damages in Table 6, respectively. At the same time, the mean relative error (MRE) was utilized to quantify the localization performance of these five models. The MRE can be expressed as

$$MRE = \frac{1}{n} \sum_{i=1}^n \sqrt{\frac{(x_A^i - x_P^i)^2 + (y_A^i - y_P^i)^2}{L}} \times 100\% \quad (12)$$

where (x_A^i, y_A^i) denotes the actual damage location, and (x_P^i, y_P^i) denotes the predicted damage location of the i -th testing datasets. The MRE reflects the mean relative localization error of all test cases, and the smaller the value is, the better the localization performance is.

Fig. 13 shows the results assessed by the MRE coefficient under the training datasets with different sizes. It is clearly observed that, in the initial stage, the training datasets increase, the MRE decreases rapidly,

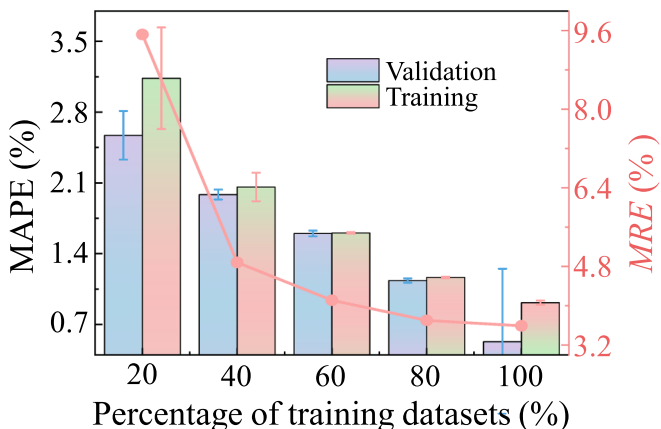


Fig. 13. Diagnosis results using various percentages of training datasets.

and then the trend of decreasing MRE slows down and gradually stabilizes with the increase of training datasets. This indicates that, to a certain extent, the prediction results obtained by the GAF-CNN-CBAM model are more accurate as the training datasets increase.

5.3.2. Effects of skip length N

The length of the damage sequence obtained by the improved PAA algorithm is mainly influenced by the length M and the skip length N as shown in Eq. (7). Therefore, the damage localization performance of the model under different skip lengths (N s) were further investigated. Here, M is set to the length of the five-cycle tone-burst excitation signal ($M = 550$), and the skip lengths (N s) are the optimal values 100, 180, 260, 340 and 420. The damage sequence length of each sensing path after compression and the damage sequence length after multi-path fusion are obtained according to Eq. (7) for five different cases, and the results are shown in Table 7.

These five different lengths of damage sequences were GAF and input into the GAF-CNN-CBAM model for training, and five trained models were obtained. The diagnosis results of the five well-trained models are displayed in Fig. 14. In this figure, the training MAPEs and validation MAPEs are also averaged by three trials, and the error bars show the standard deviations. It can be clearly observed that the MAPE values of the model first decrease and then increase with increasing skip length N , and the case 2 shows the best performance with the minimum MAPE values (1.00 percent MAPE in training and 0.95 percent MAPE in validation). Then, the five well-trained models were also used to predict the eight damages in Table 6, respectively. Fig. 14 shows the results assessed by the MRE coefficients under the different skip lengths (N s). The change in MRE values is similar to the change in MAPE values, and the best result is also obtained in case 2 with MRE value of 3.59%. This indicates that the highest damage localization accuracy is obtained by the GAF-CNN-CBAM model when N is 180.

5.4. Comparison with other state-of-the-art methods

To further prove the superiority of the proposed GAF-CNN-CBAM method, the proposed method is compared with other state-of-the-art CNN-based damage localization methods. Zhang et al. [27] has used a 1-D CNN to construct a non-linear mapping relationship between the time-varying features and the damage locations to achieve damage localization. Rautela et al. [31] has used the CWT to convert the GW signal into a time-frequency image, and input the time-frequency image into a 2-D CNN for training to establish the relationship between the image information and the damage location and achieve the localization of damage. Both methods have obtained excellent damage localization results. In this paper, the two methods were implemented and tested on the same test set. Besides, the localization performance of the model was also investigated after freezing the CBAM in the GAF-CNN-CBAM model, and the model GAF-CNN was named. The damage localization results of different methods in the middle region and edge region of the CFRP plate are detailed in Fig. 15. Obviously, the method proposed in this paper performs superior to other methods.

To provide a better visualization of the localization effect of these four methods, the MRE s were also used to quantify the localization performance. The comparison results of MRE s and MAPEs for different damage localization methods are plotted as shown in Fig. 16. It can be

Table 7
Damage sequence length at different skip lengths.

Case	M	N	One-path length	Multi-path fusion length
1	550	100	40	480 (40 × 12)
2	550	180	22	264 (22 × 12)
3	550	260	16	192 (16 × 12)
4	550	340	12	144 (12 × 12)
5	550	420	10	120 (10 × 12)

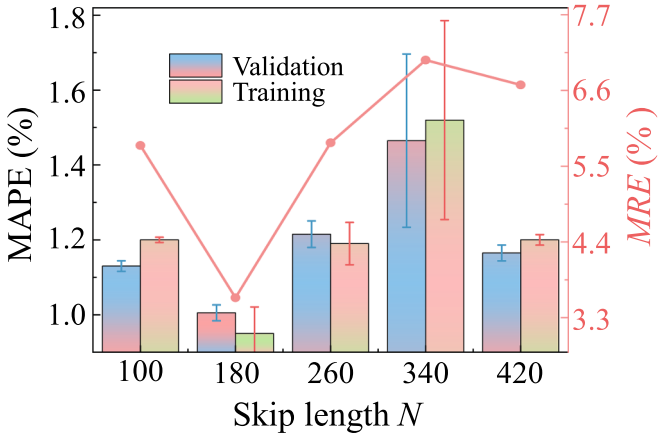


Fig. 14. Diagnosis results using various skip length N .

seen that the GAF-CNN-CBAM method has lower MRE and MAPE with MRE value of 3.59% and MAPE value of 0.38%, which means that the proposed method performs better on damage localization than the other four methods.

Additionally, the proposed method was also compared with the reconstruction algorithm for probabilistic inspection of damage (RAPID) [54]. As shown in Fig. 17(a)–(d), four cases with damages located at different locations on the CFRP plate are presented with the RAPID

method. The errors between the predicted locations and the actual locations are large especially for the damages located outside the region covered by propagation paths. This is because the number of sensors is too few for the RAPID method to work effectively. Compared with the RAPID method, the proposed method in this paper obtains better localization results as shown in Fig. 17(e)–(h). The MRE and MAPE results of the RAPID method are also presented as shown in Fig. 16.

The key reasons why the proposed method demonstrates better results than other state-of-the-art methods are mainly in three aspects: firstly, the improved PAA algorithm not only effectively reduces the redundant dimension of the GW signals, but also obtains a damage feature sequence that retains the damage time information. Therefore, it is more accurate in damage localization than the method of directly training the neural network using the raw GW signals. Secondly, the GAF image transformation preserves the temporal information of the original data effectively, which makes it easier for the GAF-CNN-CBAM to establish a nonlinear mapping relationship between the GAF image and the damage location. Finally, the innovation of using a CBAM to empower CNN to reduce its dependence on external information, enhances the network's performance to capture the internal correlation of data or features. These three aspects work in concert to help the network extract the temporally informative features of the damage from the input GAF images, making subsequent regression easier. This also explains why the localization performance of GAF-CNN is much worse than that of the GAF-CNN-CBAM model. Since the loss of the CBAM module, the existing CNN model cannot capture the damage information in GAF

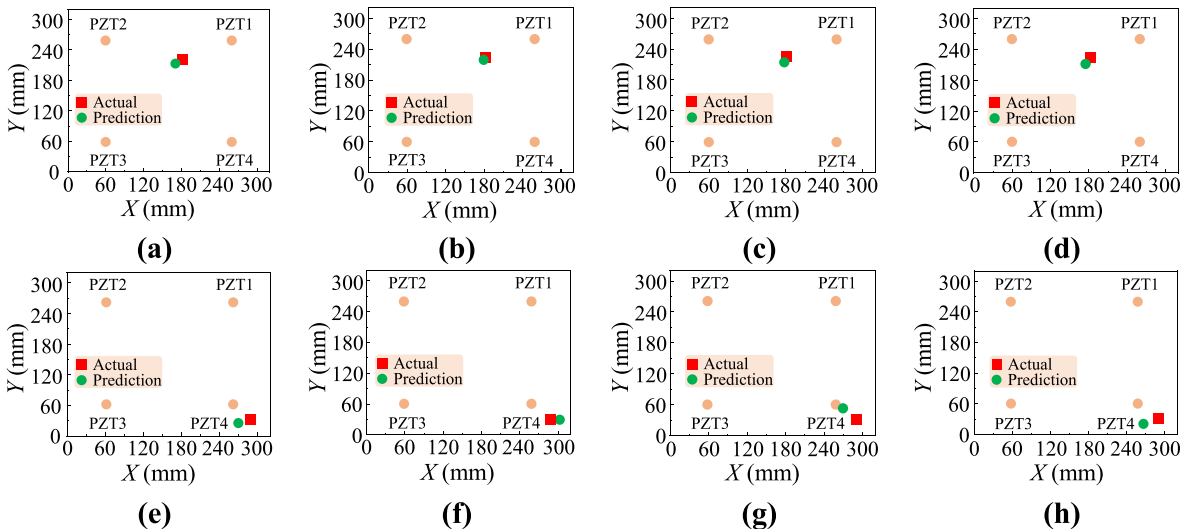


Fig. 15. Examples of the visualization of damage localization results by different methods. (a) GAF-CNN, (b) GAF-CNN-CBAM, (c) Rautela [31], (d) Zhang [26], (e) GAF-CNN, (f) GAF-CNN-CBAM, (g) Rautela [31], (h) Zhang [26].

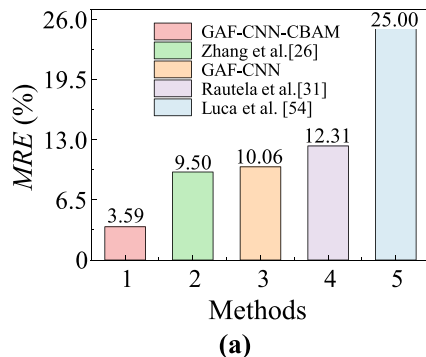


Fig. 16. Comparison of the proposed method with other state-of-the-art methods. (a) MRE, (b) MAPE.

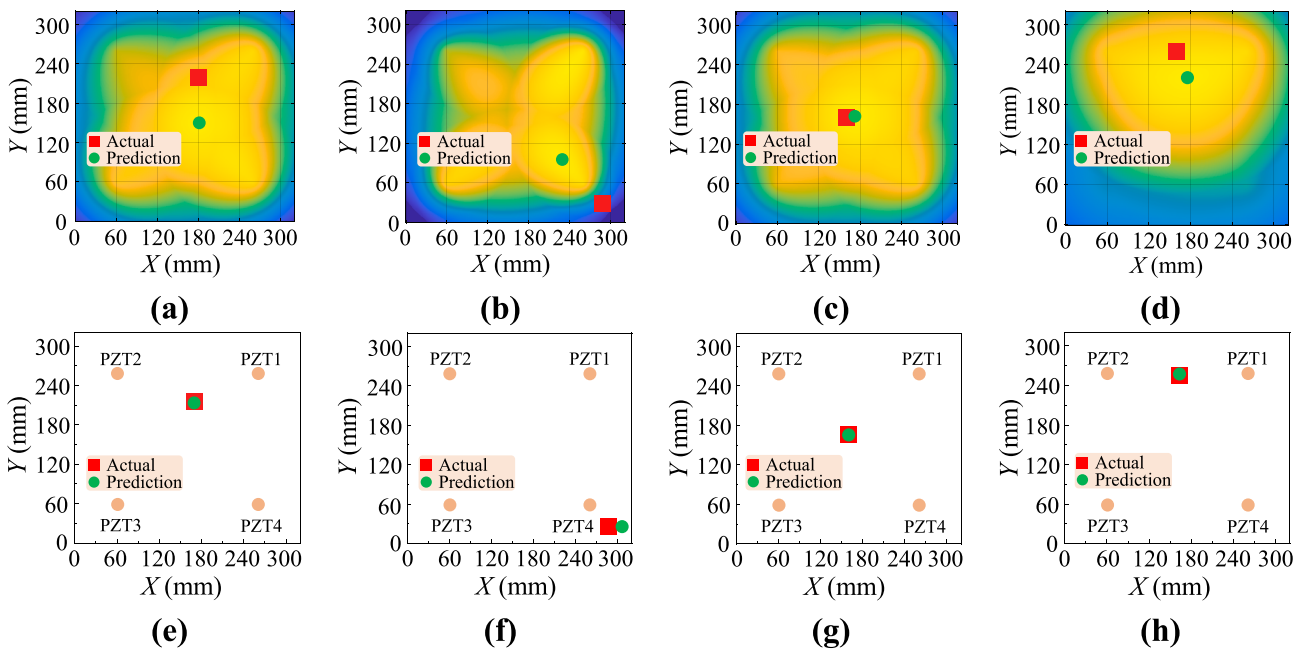


Fig. 17. Examples of the visualization of damage localization results by different methods. (a)–(d) RAPID [54], (e)–(h) GAF-CNN-CBAM.

images more effectively.

6. Conclusions

A novel damage diagnosis framework, combining GAF and CNN, has been presented, in order to improve the damage localization performance in composite structures. Experiments were carried out on composite structures using only four PZTs to validate the proposed method. Compared with other state-of-the-art damage localization methods, the proposed method has better localization performance. Based on the comprehensive and detailed comparison, the conclusions are highlighted as follows:

- (1) The improved PAA algorithm effectively preserves the feature information of the damage while reducing the dimensionality of the GW data.
- (2) The GAF image digital coding techniques combined with CNN are feasible for damage localization in composite structures.
- (3) Embedding CBAM into a CNN can effectively improve the robustness and localization performance of the network, as evidenced by the lower MSE, MAPE, MAE, and higher R^2 of the network.
- (4) The powerful regression performance of GAF-CNN-CBAM can be used to accurately identify the location of damage in composite structures and to avoid time-consuming and complex GW signal processing.

Although the developed damage localization method combining the novel GAF methodology with CNN algorithm shows some advantages, some more investigations need to be further performed. For instance, the influence of environmental factors (e.g., temperature, humidity, etc.) was not considered in the current method, and only the localization of single damage, but not multiple damages, was considered in GAF-CNN-CBAM. Therefore, considering environmental factors and multiple damages will be the significant direction of our future research.

CRediT authorship contribution statement

Yunlai Liao: Conceptualization, Methodology, Software, Data curation, Validation, Formal analysis, Writing – original draft, Writing –

review & editing. **Xinlin Qing:** Conceptualization, Supervision, Methodology, Funding acquisition, Resources, Writing – review & editing. **Yihan Wang:** Data curation, Validation. **Fanghong Zhang:** Methodology, Funding acquisition, Writing – review & editing.

Declaration of Competing Interest

The authors declare that they have no known competing financial interests or personal relationships that could have appeared to influence the work reported in this paper.

Data availability

The authors do not have permission to share data.

Acknowledgment

This work is supported by the National Natural Science Foundation of China (Grant Nos. U2141245, 11972314, 11472308), and the Foundation Project of Chongqing Normal University (Grant No. 22XLB008).

References

- [1] Yu Y, Liu X, Wang Y, et al. Lamb wave-based damage imaging of CFRP composite structures using autoencoder and delay-and-sum. *Compos Struct* 2023;303:116263.
- [2] Zeng X, Liu X, Yan J, et al. Lamb wave-based damage localization and quantification algorithms for CFRP composite structures. *Compos Struct* 2022;295:115849.
- [3] Qing X, Liao Y, Wang Y, et al. Machine learning based quantitative damage monitoring of composite structure. *Int J Smart Nano Mater* 2022;13:167–207.
- [4] Li G, Chattopadhyay A. Multi-dimensional signal processing and mode tracking approach for guided wave based damage localization in X-COR sandwich composite. *Mech Syst Sig Process* 2018;109:134–49.
- [5] Azuara G, Barrera E, Ruiz M, et al. Damage detection and characterization in composites using a geometric modification of the RAPID algorithm. *IEEE Sens J* 2020;20:2084–93.
- [6] Hong M, Su Z, Lu Y, et al. Locating fatigue damage using temporal signal features of nonlinear Lamb waves. *Mech Syst Sig Process* 2015;60–61:182–97.
- [7] Zhu J, Qing X, Liu X, et al. Electromechanical impedance-based damage localization with novel signatures extraction methodology and modified probability-weighted algorithm. *Mech Syst Sig Process* 2021;146:107001.
- [8] Thalapil J, Sawant S, Tallur S, et al. Guided wave based localization and severity assessment of in-plane and out-of-plane fiber waviness in carbon fiber reinforced composites. *Compos Struct* 2022;297:115932.

- [9] Mitra M, Gopalakrishnan S. Guided wave based structural health monitoring: a review. *Smart Mater Struct* 2016; 25: 053001(27pp).
- [10] Qing X, Li W, Wang Y, et al. Piezoelectric transducer-based structural health monitoring for aircraft applications. *Sensors* 2019;19:545.
- [11] Luca A, Perfetto D, Fenza A, et al. Guided waves in a composite winglet structure: numerical and experimental investigations. *Compos Struct* 2019;210:96–108.
- [12] Hua J, Zhang H, Miao Y, et al. Modified minimum variance imaging of Lamb waves for damage localization in aluminum plates and composite laminates. *NDT & E Int* 2022;125:102574.
- [13] Wang Y, He M, Sun L, et al. Weighted adaptive Kalman filtering-based diverse information fusion for hole edge crack monitoring. *Mech Syst Sig Process* 2022; 167:108534.
- [14] Wilson C, Chang F. Monitoring fatigue-induced transverse matrix cracks in laminated composites using built-in acousto-ultrasonic techniques. *Struct Health Monit* 2016;15:335–50.
- [15] Lim H, Lee H, Skinner T, et al. Fatigue damage detection and growth monitoring for composite structure using coda wave interferometry. *Struct Control Health Monit* 2020;28:e2689.
- [16] Li W, Cho Y. Quantification and imaging of corrosion wall thinning using shear horizontal guided waves generated by magnetostrictive sensors. *Sens Actuators, A* 2015;232:251–8.
- [17] Sikdar S, Banerjee S. Identification of disbond and high density core region in a honeycomb composite sandwich structure using ultrasonic guided waves. *Compos Struct* 2016;152:568–78.
- [18] Fenza A, Sorrentino A, Vitiello P. Application of artificial neural networks and probability ellipse methods for damage detection using lamb waves. *Compos Struct* 2015;133:390–403.
- [19] Yu Y, Liu X, Li J, et al. Life-cycle health monitoring of composite structures using piezoelectric sensor network. *Smart Mater Struct* 2021; 31: 015033(16pp).
- [20] Liu H, Liu S, Liu Z, et al. Data-driven approaches for characterization of delamination damage in composite materials. *IEEE Trans Ind Electron* 2021;68: 2532–42.
- [21] Yang B, Xuan F, Chen S, et al. Damage localization and identification in WGF/epoxy composite laminates by using Lamb waves: experiment and simulation. *Compos Struct* 2017;165:138–47.
- [22] Liu X, Tian S, Tao F, et al. A review of artificial neural networks in the constitutive modeling of composite materials. *Compos B Eng* 2021;224:109152.
- [23] Ahmed O, Wang X, Tran M, et al. Advancements in fiber-reinforced polymer composite materials damage detection methods: towards achieving energy-efficient SHM systems. *Compos B Eng* 2021;223:109136.
- [24] Khan A, Khalid S, Raouf I, et al. Autonomous assessment of delamination using scarce raw structural vibration and transfer learning. *Sensors* 2021;21:6239.
- [25] Khan A, Raouf I, Noh Y, et al. Autonomous assessment of delamination in laminated composites using deep learning and data augmentation. *Compos Struct* 2022;290:115502.
- [26] Zhang H, Peng L, Zhang H, et al. Phased array ultrasonic inspection and automated identification of wrinkles in laminated composites. *Compos Struct* 2022;300: 116170.
- [27] Zhang S, Li C, Ye W. Damage localization in plate-like structures using time-varying feature and one-dimensional convolutional neural network. *Mech Syst Sig Process* 2021;147:107107.
- [28] Pandey P, Rai A, Mitra M. Explainable 1-D convolutional neural network for damage detection using Lamb wave. *Mech Syst Sig Process* 2022;164:108220.
- [29] Rai A, Mitra M. Lamb wave based damage detection in metallic plates using multi-headed 1-dimensional convolutional neural network. *Smart Mater Struct* 2021; 30: 035010 (20pp).
- [30] Kiranyaz S, Avci O, Abdeljaber O, et al. 1D convolutional neural networks and applications: a survey. *Mech Syst Sig Process* 2021;151:107398.
- [31] Rautela M, Gopalakrishnan S. Ultrasonic guided wave based structural damage detection and localization using model assisted convolutional and recurrent neural networks. *Expert Syst Appl* 2021;167:114189.
- [32] Wu J, Xu X, Liu C, et al. Lamb wave-based damage detection of composite structures using deep convolutional neural network and continuous wavelet transform. *Compos Struct* 2021;276:114590.
- [33] Azuara G, Ruiz M, Barrera E. Damage localization in composite plates using wavelet transform and 2-D convolutional neural networks. *Sensors* 2021;21:5825.
- [34] Wen L, Li X, Gao L, et al. A new convolutional neural network-based data-driven fault diagnosis method. *IEEE Trans Ind Electron* 2018;65:5990–8.
- [35] Liu J, Ardabiliyan M, Zine A, et al. Crack damage identification of a thick composite sandwich structure based on Gaussian Processes classification. *Compos Struct* 2021;255:112825.
- [36] Cui R, Azuara G, Francesco L, et al. Damage imaging in skin-stringer composite aircraft panel by ultrasonic-guided waves using deep learning with convolutional neural network. *Struct Health Monit* 2021;1:1–16.
- [37] Tibaduiza D, Vitola J, Anaya M, et al. A damage classification approach for structural health monitoring using machine learning. *Complexity* 2018;2018:1–14.
- [38] Rautela M, Senthilnath J, Moll J, et al. Combined two-level damage identification strategy using ultrasonic guided waves and physical knowledge assisted machine learning. *Ultrasonics* 2021;115:106451.
- [39] Sikdar S, Liu D, Kundu A. Acoustic emission data based deep learning approach for classification and detection of damage-sources in a composite panel. *Compos B Eng* 2022;228:109450.
- [40] Wang S, Luo Z, Shen P, et al. Graph-in-graph convolutional network for ultrasonic guided wave-based damage detection and localization. *IEEE Trans Instrum Meas* 2022;71:1–11.
- [41] Xu Y, Zhou H, Cui Y, et al. Full scale promoted convolution neural network for intelligent terahertz 3D characterization of GFRP delamination. *Compos B Eng* 2022;242:110022.
- [42] Lecun Y, Bottou L, Bengio Y, et al. Gradient-based learning applied to document recognition. *Proc IEEE* 1998; 86: 2278–324.
- [43] Woo S, Park J, Lee J, et al. CBAM: convolutional block attention module. In: Proceedings of the European Conference on Computer Vision (ECCV), vol. 11211; 2018. p. 3–19.
- [44] Keogh E, Chakrabarti K, Pazzani M, et al. Dimensionality reduction for fast similarity search in large time series databases. *Knowl Inf Syst* 2001;3:263–86.
- [45] Hu M, He J, Zhou C, et al. Surface damage detection of steel plate with different depths based on Lamb wave. *Measurement* 2022;187:110364.
- [46] Lei Y, Jia F, Lin J, et al. An intelligent fault diagnosis method using unsupervised feature learning towards mechanical big data. *IEEE Trans Ind Electron* 2016;63: 3137–47.
- [47] Wang Z, Oates T. Imaging time-series to improve classification and imputation. In: Proceedings of the Twenty-Fourth International Joint Conference on Artificial Intelligence; 2015. p. 3939–45.
- [48] Moll J, Kathol J, Fritzen C, et al. Open guided waves: online platform for ultrasonic guided wave measurements. *Struct Health Monit* 2018;18:1903–14.
- [49] Ewald V, Goby X, Jansen A, et al. Batch normalization: Accelerating deep network training by reducing internal covariate shift. In: 10th Intl Symposium on NDT in Aerospace, Dresden; 2018. p. 1–9.
- [50] Shorten C, Khoshgoftaar T. A survey on image data augmentation for deep learning. *J Big Data* 2019;6(60):1–48.
- [51] Kingma D, Ba J. Adam: a method for stochastic optimization. Published as a conference paper at ICLR 2015; 2015.
- [52] Su C, Jiang M, Liang J, et al. Damage localization of composites based on difference signal and lamb wave tomography. *Materials* 2020;13:218.
- [53] Malekloo A, Ozer E, AlHamaydeh M, et al. Machine learning and structural health monitoring overview with emerging technology and high-dimensional data source highlights. *Struct Health Monit* 2021;1–50.
- [54] Luca A, Perfetto D, Fenza A, et al. Guided wave SHM system for damage detection in complex composite structure. *Theor Appl Fract Mech* 2020;105:102408.